

# On the boundary cost of source-consistent warp shells

An T. Le<sup>1,2,3</sup>

<sup>1</sup>Center for Environmental Intelligence, VinUniversity, Hanoi, Vietnam

<sup>2</sup>College of Engineering and Computer Sciences, VinUniversity, Hanoi, Vietnam

<sup>3</sup>Intelligent Autonomous Systems, TU Darmstadt, Germany

**E-mail:** an.lt@vinuni.edu.vn; an@robot-learning.de

---

## Abstract

We study classical energy-condition admissibility for subluminal, positive-energy warp shells. For the constructions examined here, the energy-condition failures are localized at the smooth source–vacuum transition rather than in the bulk interior. We introduce two *source-first* shell ansätze whose metric potentials are obtained from the Einstein constraints for a prescribed matter model: a shift-free S-shell and a T-shell whose shift is derived from the momentum constraint. We assess them with a five-criterion standard comprising regularity, constraint satisfaction, an explicit matter model, frame-independent energy-condition margins, and global diagnostics; the standard responds to the source-consistency critique of Barzegar, Buchert, and Vigneron. Applied to eight constructions spanning the canonical warp-drive classes, none passes the full standard. An independent frame-independent verification of the Fuchs constant-velocity shell confirms interior energy-condition compliance (0 of 13 interior probes violate) but reveals Hawking–Ellis Type IV violations in the smoothing tail beyond the nominal shell. A frame-independent scan over shell compactness and thickness (600 configurations) yields no admissible configuration in either source-first class. The same boundary deficit appears in the shift-free S-shell and persists in the static  $v_0 = 0$  limit, which ties it to the transition geometry rather than to the shift. Along a representative off-axis null ray the null-energy line integral is nevertheless positive for every source-prescribed shell; this is an exploratory diagnostic rather than a proof of the averaged null energy condition, but it shows that the pointwise boundary failures need not appear in that integral.

**Keywords:** warp drive, energy conditions, general relativity, exact solutions, Einstein constraints

---

## 1 Introduction

The search for physically viable warp-drive spacetimes has been reinvigorated by constructions that report satisfaction of the classical energy conditions (ECs) at subluminal bubble velocities [1–4]. These reports must be set against a body of no-go results: Pfenning and Ford [5] showed that the original Alcubierre construction requires negative energy of order  $10^{11}$  visible-universe masses for its original bubble parameters (the bound is parameter-dependent); Ford and Roman [6] established quantum-inequality bounds; Flanagan and Wald [7] analyzed the averaged null energy condition (ANEC); and Lobo and Visser [8] derived fundamental limitations on warp-drive spacetimes. Together these establish a baseline obstruction: non-trivial spacetime transport conflicts with the pointwise classical energy conditions in the absence of exotic matter sources [9, 10], and superluminal transport in particular requires negative energy by the Olum [11] no-go, so we restrict throughout to subluminal configurations. A companion paper [12] introduced WARPAX, a JAX-based toolkit that certifies energy-condition margins over the family of timelike observers using the Hawking–Ellis algebraic classification [13] together with continuous optimization. That work found that single-frame (Eulerian) analysis can miss 15–28% of DEC-violating grid points, which is why we treat frame-independent certification as the relevant test rather than an optional refinement.

The 2021–2024 wave of subluminal positive-energy proposals (Lentz’s diamond soliton [14], the Bobrick–Martire general framework [1], and the Fuchs *et al.* constant-velocity shell [2]) revived the question of whether subluminal constructions can satisfy the classical energy conditions in the Eulerian frame; recent extensions place warp bubbles in de Sitter backgrounds that satisfy the averaged conditions under matched expansion [15]. Each construction has since been scrutinized. Santiago, Schuster, and Visser [16] established that generic warp drives violate the null energy condition, and that observer-dependent EC margins can mask Eulerian-frame compliance; Celmaster and Rubin [17] identified algebraic errors in the Lentz WEC derivation; and the

Barzegar–Buchert–Vigneron classification and follow-up [18, 19] argued that the metric-first ( $G$ -method) constructions on which most of these proposals rest carry structural problems that go beyond pointwise EC tests: a matter flow constrained to lie in the time slice, a spatial curvature that is suppressed by construction, and velocity fields whose interpretation depends on the coordinates.

This paper addresses *source consistency*: whether a warp metric solves a well-posed Einstein system for physically meaningful matter, not merely whether it satisfies the energy conditions. The formal critiques of Barzegar, Buchert, and Vigneron [18–20] argue that unrestricted metric-first construction (prescribing  $g_{ab}$  and computing  $T_{ab} = G_{ab}/8\pi$ ) can produce “fantastic” stress-energy tensors that do not correspond to physically meaningful matter. Their analysis identifies specific pathologies: a required orthogonality of the matter flow to the time slice, a vanishing spatial Ricci tensor that excludes genuine spatial curvature, and coordinate-dependent velocity fields that carry no covariant meaning. Each of these challenges the interpretation of the construction as real matter. Energy-condition satisfaction alone is therefore insufficient; an admissible construction must solve the Einstein constraint equations for an interpretable source model.

We make four contributions. First, we propose a five-criterion admissibility standard (regularity, Einstein constraint satisfaction, an explicit matter model, frame-independent energy-condition margins, and global diagnostics; Sec. 2) that responds to the Barzegar–Buchert–Vigneron critique by demanding physical interpretability of the matter rather than only EC satisfaction of the metric. Second, we construct two source-first shell ansätze, the shift-free S-shell (Sec. 6) and the T-shell with a constraint-derived shift (Sec. 7), whose metric potentials follow from a quasi-static reduction of the Einstein constraints for a prescribed matter model and are then verified against the full constraints (Fig. 1); both satisfy the Hamiltonian constraint to  $\epsilon_{\mathcal{H}} \sim 10^{-6}$ , well below the energy-condition margins, with positive interior EC margins and only a residual boundary failure. Third, we report an independent frame-independent verification of the Fuchs constant-velocity shell [2] (Sec. 4): reproducing the construction via iterative Gaussian-kernel smoothing [21, 22], we find 22 of 25 transition-tail Type IV violations that are not visible to an Eulerian analysis [16], and applying the same standard to the Rodal [3], Lentz [14], Alcubierre, Natário, and Van den Broeck proposals (Sec. 5) leaves none passing. Fourth, a  $20 \times 15$  scan over compactness and thickness for both shells (600 grid points, Sec. 8) finds no admissible configuration, consistent with the Lobo–Visser obstruction [8] across this surveyed family under the stricter frame-independent standard.

Throughout we work in geometric units ( $G = c = 1$ ) with signature  $(-+++)$ .

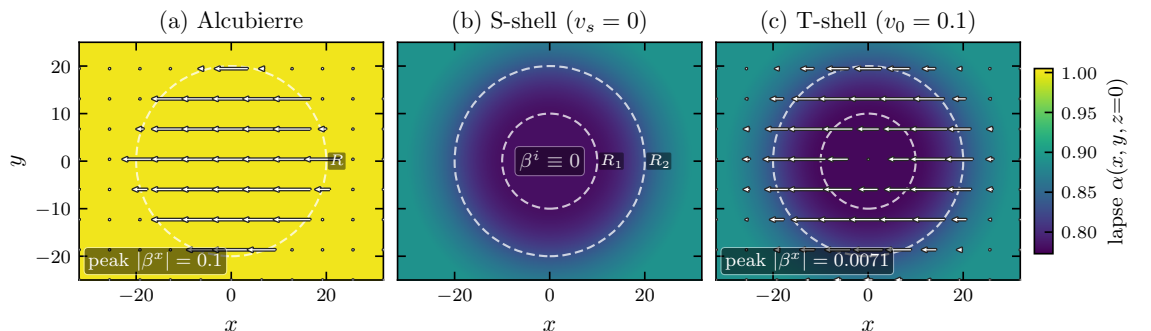


**Figure 1.** The three constructions on the  $z = 0$  slice. Color field: lapse  $\alpha(x, y, z=0)$  (shared colorbar). White arrows: shift vector field  $\beta^i$ , auto-scaled per panel for legibility, so the annotated peak  $|\beta^x|$  (not the arrow length) carries the cross-panel magnitude comparison. Dashed circles: characteristic radii. (a) Alcubierre (kinematic, metric-first;  $v_s = 0.1$ ,  $R = 20$ ,  $\sigma = 2$ ): unit lapse with a gauge-engineered shift bubble of radius  $R$ ; transport is encoded entirely in  $\beta^i$ . (b) S-shell (source-first, static): lapse depression in the spherical shell  $[R_1, R_2]$  derived from the Hamiltonian constraint for a prescribed isotropic source; the shift vanishes by construction. (c) T-shell (source-first, kinematic): the same source-derived lapse pocket as the S-shell, with the shift  $\beta^x$  a solution of the momentum constraint for a tilted matter 4-velocity ( $v_0 = 0.1$ ). Its peak shift (0.0071) is more than an order of magnitude below Alcubierre’s (0.1), consistent with being constraint-derived rather than postulated by a coordinate ansatz.

## 2 Admissibility standard

In response to the Barzegar–Buchert–Vigneron critique, we formalize physical viability through five criteria; a warp-shell candidate is *admissible* only if it satisfies all five.

**A. Regularity.** The metric must satisfy  $g_{ab} \in C^2$  for thick-shell constructions, so that the Einstein tensor is classically well-defined. For thin shells, the Israel junction conditions and the associated surface stress-energy replace the bulk  $G_{ab}$  [23].

**B. Constraint satisfaction.** The Hamiltonian and momentum constraints encode energy and momentum conservation on the initial slice, and the initial data  $(\gamma_{ij}, K_{ij})$  must satisfy both:

$$\mathcal{H} = R(\gamma) + K^2 - K_{ij}K^{ij} - 16\pi E = 0, \quad (1)$$

$$\mathcal{M}_i = D_j(K^j_i - \delta^j_i K) - 8\pi S_i = 0. \quad (2)$$

We compute normalized residuals  $\epsilon_{\mathcal{H}}$  and  $\epsilon_{\mathcal{M}}$  following the conventions of Ref. [12] (see Sec. 3). Metric-first constructions satisfy (1)–(2) tautologically, because one *defines*  $T_{ab} = G_{ab}/8\pi$ ; criterion B is therefore informative only when the source is prescribed independently and the metric potentials are obtained by solving the constraints, as in the S-shell and T-shell ansätze of Secs. 6–7.

**C. Explicit matter model.** The source must represent physical matter (an anisotropic fluid, an elastic shell, or a scalar/vector field), not an abstract stress-energy tensor. This criterion responds directly to Barzegar *et al.* [18]: the  $G$ -method exhibits a stress-energy tensor without constraining the matter it represents.

**D. Frame-independent EC margins.** We certify the NEC, WEC, and DEC margins with WARPAX. We use the term *observer-robust* for a margin certified over the timelike-observer family rather than evaluated in a single frame: exactly, from the energy-momentum eigenvalues, at Hawking–Ellis Type I [13] points, and through a bounded-rapidity multi-start search elsewhere, with cap  $\zeta_{\max} = 5$  (maximum Lorentz factor  $\gamma_{\max} = \cosh \zeta_{\max} \approx 74$ ). The margins are stable across the convergence sweep  $\zeta_{\max} \in \{1, 3, 5, 7\}$  for the Alcubierre baseline at  $v_s = 0.5$ , with the full convergence study in Ref. [12]. All margins must be non-negative at every radial probe across the support of non-negligible stress-energy: the bulk shell  $[R_1, R_2]$  for compact-support constructions, extended to the immediate smoothing tail where matter remains non-negligible (for the Gaussian-smoothed Fuchs construction, 25 exterior probes covering  $r \in [R_2, R_2 + \sim 6\sigma]$ ). We omit the strong energy condition (SEC) from criterion D because cosmologically realistic positive-pressure and dark-energy components routinely violate it, and because anisotropic stresses generically violate SEC without rendering the matter unphysical [9, 10].

**E. Global and invariant diagnostics.** Positive ADM mass, passenger-cavity tidal forces below a safety threshold, and at least one invariant transport observable (geodesic deviation, null round-trip asymmetry, or blueshift hazard; necessarily absent for the static, shift-free S-shell baseline, where the verdict rests on mass and tidal forces). Asymptotic  $1/r$  falloff is verified separately as a diagnostic: it holds exactly for the source-first shells with strict compact support on  $[R_1, R_2]$ , and approximately for the Gaussian-smoothed Fuchs construction whose smoothing tail extends matter beyond  $R_2$ .

## 3 Methods

### 3.1 Energy-condition certification

Criterion D is the computationally demanding step: it requires continuous optimization over the timelike-observer family to estimate worst-case violations rather than sampling a fixed observer set. We use multi-start BFGS over the bounded rapidity  $\zeta \leq \zeta_{\max}$ , which is exact for Hawking–Ellis Type I points (where the EC sign is fixed by the energy-momentum eigenvalues) and heuristic for Type II–IV points (where local minima are possible); we state this status explicitly wherever it affects a verdict. The curvature chain is built by forward-mode automatic differentiation through JAX [24] with 64-bit arithmetic. We implement the analysis in WARPAX [12], extending the toolkit with the source-consistency capabilities required by criteria B–E: Hamiltonian and momentum constraint residuals, anisotropic TOV equilibrium, Israel–Darmois surface stress-energy, ADM mass with asymptotic-falloff verification, and the invariant transport diagnostics above.

From the Type I eigenvalues  $(\rho, p_1, p_2, p_3)$  of  $T^a_b$  the signed margins are

$$\begin{aligned} \text{NEC} &= \min_i(\rho + p_i), & \text{WEC} &= \min(\rho, \min_i(\rho + p_i)), \\ \text{DEC} &= \min_i(\rho - |p_i|), \end{aligned} \quad (3)$$

positive when the condition holds. At non-Type I points the same quantities are minimized over the bounded-rapidity observer family.

### 3.2 Source-first shell construction

Both source-first shells are built on the spherical 3+1 (ADM) line element

$$ds^2 = -\alpha(r)^2 dt^2 + \gamma_{ij} (dx^i + \beta^i dt)(dx^j + \beta^j dt), \quad (4)$$

with lapse  $\alpha = e^{\Phi(r)}$ , spatial metric  $\gamma_{ij} = \delta_{ij} + (e^{2\Lambda(r)} - 1) \hat{r}_i \hat{r}_j$  where  $\hat{r}_i = x_i/r$  is the unit radial covector, and shift  $\beta^i$  that vanishes for the S-shell and is purely  $\beta^x(r)$  for the T-shell. We prescribe a tilted perfect-fluid source with 4-velocity  $u^a = \Gamma(n^a + v^a)$ ,  $v^a n_a = 0$ ,  $\Gamma = (1 - v^2)^{-1/2}$ , where  $n^a$  is the unit normal to the time slice; its Eulerian projections are

$$E = \Gamma^2(\rho + p v^2), \quad S_i = \Gamma^2(\rho + p) v_i, \quad S_{ij} = \Gamma^2(\rho + p) v_i v_j + p \gamma_{ij}. \quad (5)$$

The S-shell is the  $v = 0$ , isotropic limit ( $E = \rho$ ,  $S_i = 0$ ).

Spherical reduction of the Hamiltonian constraint (1) gives the radial potential in closed form,

$$e^{2\Lambda(r)} = \frac{1}{1 - 2m(r)/r}, \quad m(r) = 4\pi \int_0^r E(r') r'^2 dr', \quad (6)$$

and the lapse follows from quasi-static hydrostatic (TOV) equilibrium,

$$\frac{d\Phi}{dr} = \frac{m + 4\pi r^3 p_{\text{eff}}}{r(r - 2m)}, \quad \Phi(r_{\text{max}}) = \frac{1}{2} \ln(1 - 2M/r_{\text{max}}), \quad (7)$$

integrated inward from the Schwarzschild exterior, with  $p_{\text{eff}} = p_r$  for the S-shell and  $p_{\text{eff}} = \Gamma^2(\rho + p) v^2 + p$  for the T-shell. The S-shell radial pressure itself solves the anisotropic TOV equation  $dp_r/dr = -(\rho + p_r)(m + 4\pi r^3 p_r)/[r(r - 2m)]$  with  $p_r(R_2) = 0$ . For the T-shell we do not postulate the shift; we obtain it from the momentum constraint (2), which reduces to the linear boundary-value problem

$$\beta'' + A(r) \beta' + B(r) \beta = 8\pi \alpha S_x, \quad A = \frac{2}{r} + 2\Phi' - 2\Lambda', \quad B = -\frac{2}{r^2}, \quad (8)$$

with  $\beta'(0) = 0$  (regularity) and  $\beta(r_{\text{max}}) = 0$  (asymptotic flatness), solved as a tridiagonal system. The constraint solvers are formulated as pure tridiagonal boundary-value problems, giving end-to-end differentiability of the metric potentials with respect to the source profiles.

The source profiles are parameterized with Bernstein polynomials of compact support on  $[R_1, R_2]$ ,

$$\rho(r) = \rho_0 \sum_{a=0}^{n-1} c_a^\rho B_a^{n-1} \left( \frac{r - R_1}{R_2 - R_1} \right), \quad (9)$$

with  $c_0^\rho = c_{n-1}^\rho = 0$  enforcing compact support and analogous expansions for the pressures and the velocity profile. The shell joins the vacuum exterior through a  $C^2$  smoothstep  $S(t) = 6t^5 - 15t^4 + 10t^3$  ( $S, S', S''$  matched at the endpoints) of width  $w = 0.05(R_2 - R_1)$ .

The normalized constraint residuals are scale-invariant ratios,

$$\epsilon_{\mathcal{H}} = \frac{|\mathcal{H}|}{\max(|R| + K^2 + K_{ij} K^{ij} + 16\pi|E|, 1)}, \quad \epsilon_{\mathcal{M}} = \frac{\|\mathcal{M}_i\|}{\max(\|\mathcal{M}_i + 8\pi S_i\| + \|8\pi S_i\|, 1)}, \quad (10)$$

evaluated against the prescribed Eulerian source ( $E, S_i$ ) of Eq. (5). Each denominator term carries the same dimensions as the constraint, so the ratio is dimensionless wherever the physical scale dominates; the floor (unity in the geometric length units set by  $R_2$ ) is a regularization that prevents division by a vanishing scale in near-vacuum regions, where both numerator and denominator collapse. The residuals quoted below are evaluated inside the shell, where the physical denominator far exceeds this floor, so they report the true relative residual. Equations (6)–(8) are the spherically reduced system we solve to *construct* the metric potentials; the residuals (10) are then evaluated against the *full* ADM constraints (1)–(2), so the shift-generated extrinsic-curvature and angular contributions that the radial reduction does not capture appear in  $\epsilon_{\mathcal{H}}$  and  $\epsilon_{\mathcal{M}}$ . In particular, for the  $x$ -tilted flow the squared velocity  $v^2 = \gamma_{xx}(v^x)^2 = [1 + (e^{2\Lambda} - 1)(x/r)^2](v^x)^2$  is angle-dependent, so the Eulerian source terms  $E$  and  $p_{\text{eff}}$  carry angular structure that the spherical reduction treats on-axis; this axisymmetric-as-spherical approximation is bounded *a posteriori* by the full three-dimensional residuals reported below ( $\epsilon_{\mathcal{H}} \sim 3 \times 10^{-6}$ ,  $\epsilon_{\mathcal{M}} \sim 4 \times 10^{-4}$ ). For the default T-shell the extrinsic-curvature part of the Hamiltonian,  $K^2 - K_{ij} K^{ij}$ , is negligible against  $16\pi E$  throughout the shell: on the static slice  $K_{ij} = (2\alpha)^{-1}(D_i \beta_j + D_j \beta_i)$  is  $\mathcal{O}(\partial\beta)$ , and the constraint-derived shift is tiny ( $|\beta^x| \lesssim 7 \times 10^{-3}$ ), so both  $K^2$  and  $K_{ij} K^{ij}$  are  $\mathcal{O}((\partial\beta)^2)$  and stay

many orders of magnitude below the matter term, as confirmed by the full 3D residual  $\epsilon_{\mathcal{H}} \sim 3 \times 10^{-6}$  that includes the exact  $K$ -terms. This is why the static reduction is a controlled approximation. We probe constraint residuals with a 2% geometric margin from each shell boundary to avoid transition-region artifacts, while EC certification probes the full shell domain  $[R_1, R_2]$  including the boundaries, with  $n_{\text{starts}} = 8$  multi-start BFGS in the scan and  $n_{\text{starts}} = 16$  for single-metric certification. We apply this framework to existing and new warp-shell proposals, beginning with the Fuchs constant-velocity shell.

## 4 Fuchs shell verification

This section verifies the Fuchs *et al.* constant-velocity physical warp shell [2], which employs anisotropic pressures, a non-unit lapse, and a smooth density profile inside a compact shell ( $R_1 = 10$ ,  $R_2 = 20$ , bubble velocity  $v_s = 0.02$ ) and which the authors report as satisfying all classical energy conditions in the Eulerian frame. We reproduce the construction in WARPAX, following the original five-step procedure: (i) a constant-density initial guess, (ii) a TOV-derived isotropic pressure, (iii) iterative smoothing with differential kernel widths ( $\sigma_\rho/\sigma_P \approx 1.72$ , applied four times), (iv) metric-function computation from Carroll Eqs. 5.143/5.152 [25], and (v) Schwarzschild boundary matching. A Gaussian kernel replaces the original MATLAB moving average (variance-matched as  $\sigma_{\text{gauss}} = s_{\text{MA}}/\sqrt{12}$ ) to obtain equivalent boundary regularization with cleaner spectral properties [21, 22]; we return to this substitution below. We then evaluate the result under the full admissibility standard (Table 1).

The canonical Gaussian-smoothed Fuchs metric passes criterion A (regularity, with  $C^2$  continuity checked on a 50-point radial sweep) and criterion E (positive total mass  $M = 2.98$ ). Under the remaining criteria:

*Constraint satisfaction (criterion B).* Evaluated against its prescribed (smoothed) source, the canonical Fuchs metric satisfies the Hamiltonian constraint to  $\epsilon_{\mathcal{H}} \approx 3 \times 10^{-8}$  and the momentum constraint to  $\epsilon_{\mathcal{M}} \approx 4 \times 10^{-4}$  across the radial sweep: it is built from the smoothed profiles through the TOV relations, so the constraint is met to solver precision, even tighter than the source-first shells of Sec. 7 on its finer analytic grid. The un-smoothed constant-density intermediate is by contrast far from a constraint solution, so the iterative smoothing is what renders the metric constraint-consistent.

*Source consistency (criterion C).* The matter model is explicit (an anisotropic fluid), so criterion C, which asks for a physical matter ansatz rather than full metric–source stress agreement, is met; what we quantify here is the finer degree of that agreement, and the pointwise mismatch is large. We compute the relative residual between the metric-derived stress-energy  $T_{ab}^{(\text{metric})} = G_{ab}/8\pi$  and the prescribed source  $T_{ab}^{(\text{source})}$  at every radial probe. The residual peaks at  $\sim 640\times$  the local  $T_{ab}$  norm in the constant-density pre-smoothing intermediate. This quantifies the Barzegar *et al.* [18] tension: the prescribed source and the metric-implied source disagree by nearly three orders of magnitude before smoothing. The smoothing reduces this to a relative residual of  $\approx 0.4$  at the inner edge ( $\approx 0.14$  shell-averaged) for the canonical metric, smaller but still appreciable, because the smoothed isotropic prescription does not reproduce the metric-implied anisotropic stress. This is the qualitative distinction from the source-first shells below, whose interior source residual stays at the  $10^{-3}$  level.

*Frame-independent EC margins (criterion D).* Inside the bulk shell ( $r \in [10, 20]$ , 13 probe points) we find 0 violations of NEC, WEC, or DEC under multi-observer certification with  $n_{\text{starts}} = 16$ ; all 13 probes are Hawking–Ellis Type I with positive margins  $\sim 8 \times 10^{-5}$ . In the smoothing tails outside the nominal shell, however, 22 of 25 exterior probes ( $r > R_2$ ) are Type IV (the stress-energy has no timelike eigenvector, so no observer finds a local rest frame), with  $\min_r(\text{WEC, DEC}) \approx -7.9 \times 10^{-3}$  (worst probe at  $r \approx 23.9$ ).

Our frame-independent evaluation agrees with the Eulerian analysis in the bulk interior: the smoothed bulk interior is EC-compliant. The certification adds information in the smoothing tails ( $r > R_2$ ), where we identify Type IV violations that an Eulerian observer does not see. This is the Santiago–Schuster–Visser mechanism [16] at work. The *location* of the binding EC failure therefore shifts under multi-observer certification: it is absent in the Eulerian bulk interior and present in the frame-independent smoothing transition tail.

Because the reported violation lives in the smoothing tail, we checked that it does not depend on our Gaussian substitution for the original MATLAB moving average. Repeating the verification with an exact variance-matched moving-average (boxcar) kernel reproduces the same tail: 22 of 25 exterior probes remain Hawking–Ellis Type IV, with a marginally deeper worst margin  $\min_r(\text{WEC, DEC}) \approx -8.2 \times 10^{-3}$  at the same radius  $r \approx 23.9$  (versus  $-7.9 \times 10^{-3}$  for the Gaussian). The transition-tail violation is therefore a property of the iterative smoothing, not an

artifact of the kernel choice.

## 5 Existing proposals under the admissibility standard

Before introducing the source-first shells, we apply the same five-criterion standard to the existing subluminal proposals of Rodal and Lentz and to the foundational Alcubierre, Natário, and Van den Broeck baselines. The failures established here are what motivate a source-first approach.

**Rodal irrotational drive [3].** This construction uses an irrotational (curl-free) shift vector derived from a scalar potential, with unit lapse and flat spatial metric. The irrotational property guarantees a globally Hawking–Ellis Type I classification and reduces the peak NEC/WEC violation by a factor of  $\sim 38$  relative to the Alcubierre baseline [3]. Evaluated against the standard: criterion A passes ( $C^\infty$  tanh profiles); criterion B is satisfied tautologically to machine precision ( $\epsilon_{\mathcal{H}} \sim 10^{-6}$ ), since the metric is prescribed and  $T_{ab} := G_{ab}/8\pi$ . Criterion C is not applicable: no source model is prescribed independently, and the stress-energy follows the  $G$ -method in the sense of Refs. [8, 18]. For criterion D, 9/50 probes violate NEC and 46/50 violate DEC under multi-observer certification: the construction concentrates EC failure in the DEC channel even though its peak NEC magnitude is  $\sim 38\times$  smaller than Alcubierre’s [3]. A recent follow-up by Rodal [26] confirms that residual NEC/WEC/DEC/SEC violations persist for irrotational Type I backgrounds even under area-metric birefringent screening, and that fast walls are disfavored, consistent with our finding. Criterion E fails with  $M_{\text{ADM}} = 0$  by construction (compact support, no  $1/r$  falloff).

**Lentz diamond soliton [14].** The Lentz soliton uses a diamond-pattern ( $L^1$ -norm) shift field with unit lapse and flat spatial metric. The original construction claims WEC satisfaction, but Celmaster and Rubin [17] have since identified algebraic errors in that derivation. We use the WarpFactory-style piecewise implementation [27]. Criterion A is met by the smooth shape function, though the  $L^1$  distance introduces  $C^1$  kinks in the WarpFactory implementation at the diamond axes, the origin of the boundary spike below; criterion B is tautologically satisfied (metric-first); criterion C is not applicable. For criterion D, our verification finds 1/50 NEC, 1/50 WEC, 1/50 SEC, and 2/50 DEC violations at the diamond boundary ( $r \approx R = 100$ ), after we regularize the on-axis derivative of  $\rho_\perp = \sqrt{y^2 + z^2}$  in the diamond shape function to avoid a coordinate-chart singularity. The remaining 49 probes are Type I, but the worst-margin magnitudes at the  $L^1$  corner are dominated by a curvature spike ( $\lesssim -10^{16}$  for NEC,  $\lesssim -10^{36}$  for DEC) generated by the WarpFactory piecewise-linear distance function, whose discontinuous derivatives concentrate curvature at the boundary. Repeating the certification with a  $C^2$  (Euclidean-distance) shape function removes the Type IV point entirely and collapses the worst margins to the optimizer noise floor ( $\gtrsim -10^{-17}$ ), so the  $10^{16}$ – $10^{36}$  magnitudes are an artifact of the  $L^1$  distance’s discontinuous derivatives, not an intrinsic property of a smoothed Lentz construction. The finding agrees with the independent Eulerian analysis of Celmaster and Rubin [17]. Criterion E fails with  $M_{\text{ADM}} = 0$ .

**Reference metric-first baselines.** To anchor the comparison across classes we also evaluate three foundational warp metrics at comparable parameters ( $v_s = 0.1$ ,  $R = 20$ ,  $\sigma = 2$ ): the original Alcubierre construction [28], the zero-expansion Natário variant [29], and the conformal-factor Van den Broeck microsphere [30]. Each is metric-first and inherits the structural pathologies discussed by Barzegar *et al.* [18]: criterion B is tautologically satisfied since  $T_{ab} := G_{ab}/8\pi$ , criterion C is not applicable absent a source prescription, and criterion E fails with  $M_{\text{total}} = 0$  by compactness. Criterion D fails in every case under multi-observer BFGS certification: on a 50-point radial sweep we find NEC/WEC/DEC violations at 18/22/25 points (Alcubierre), 29/30/35 points (Natário), and 16/24/25 points (Van den Broeck), with Hawking–Ellis Type II–IV regions in all three. These results are consistent with the Pfenning–Ford [5] quantum-inequality bounds, the Olum [11] subluminality result, and the Lobo–Visser limitations [8].

None of these six existing constructions passes the standard: the Natário-class metrics (Alcubierre, Natário, Van den Broeck, Rodal, Lentz) lack both a source model and positive ADM mass, while the Fuchs shell has both but fails criterion D in its smoothing tail. This is the gap the source-first shells are designed to close.

## 6 Source-first construction: S-shell

These failures motivate constructions derived directly from the Einstein constraints for a prescribed matter model. We introduce two such ansätze: the S-shell (this section, flow-orthogonal, zero shift)

and the T-shell (Sec. 7, tilted flow with constraint-derived shift). Both follow the Barzegar–Buchert–Vigneron prescription directly: we fix the matter, then solve for the metric using the equations of Sec. 3.2.

In the S-shell (Class I) the matter 4-velocity is aligned with the hypersurface normal  $n^a$ . The spatial metric is non-flat, the lapse non-unit ( $\alpha \approx 0.78$  in the interior), and the shell carries perfect-fluid isotropic pressure ( $p_t = p_r$ ) from hydrostatic balance; we defer anisotropic extensions to future work. Given source profiles  $\rho(r)$  and  $p(r)$ , we integrate the Hamiltonian constraint (6) for  $\Lambda(r)$  and obtain the lapse from the TOV equilibrium (7). Because we derive the metric potentials from the source rather than prescribing them, the constraint residual is limited only by solver discretization: against the prescribed source we find  $\epsilon_{\mathcal{H}} \approx 2 \times 10^{-6}$  across the shell, with  $\epsilon_{\mathcal{M}} \equiv 0$  identically (zero shift implies zero Eulerian momentum density), and the interior source-consistency residual stays at the  $10^{-3}$  level. Zero shift ( $\beta^i = 0$ ) means the S-shell carries no transport utility, but it is a physically clean baseline for criterion B. Deep-interior EC margins are positive (worst DEC  $\approx +9.4 \times 10^{-5}$ ), but a DEC violation persists at the inner boundary  $r = R_1$  with margin  $\approx -4.5 \times 10^{-4}$  (Fig. 3), of the same sign and magnitude as the T-shell inner-boundary failure (Sec. 7). This independent recurrence in the shift-free S-shell ties the boundary DEC failure to the smooth source–vacuum transition itself rather than to the shift.

## 7 Source-first construction: T-shell

We extend the S-shell to a tilted-flow construction, the T-shell (Class II): the matter 4-velocity  $u^a$  tilts relative to the hypersurface normal  $n^a$ , generating a nonzero Eulerian momentum density  $S_i$ . We do not postulate the shift vector  $\beta^x$ ; we obtain it from the momentum constraint (8) as the boundary-value solution for a prescribed velocity profile  $v_x(r)$ . This addresses the Barzegar–Buchert–Vigneron critique [18, 19] that many warp constructions employ a coordinate shift ansatz rather than genuine covariant matter motion: in the T-shell the shift is a derived consequence of how the matter flows, not a free design choice.

For the default configuration ( $R_1 = 10$ ,  $R_2 = 20$ ,  $\rho_0 = 10^{-4}$ ,  $v_0 = 0.1$ ) we find (Table 1, Fig. 4):

- Constraint residuals against the prescribed source:  $\epsilon_{\mathcal{H}} \approx 3 \times 10^{-6}$  (well below the binding outer-boundary DEC violation of order  $10^{-2}$ ) and  $\epsilon_{\mathcal{M}} \approx 4 \times 10^{-4}$ , comparable to the inner-boundary margin; the robustness study of Sec. 8 shows the violation sign survives as both residuals are reduced, so the residuals do not account for the boundary failures.
- EC margins in the deep interior: all NEC, WEC, and DEC margins are positive at probe points with 2% boundary offsets ( $r \in [10.2, 19.8]$ ), worst DEC margin  $\approx +9.3 \times 10^{-5}$ .
- EC at the shell boundaries: the T-shell carries two transition residues. An inner-boundary DEC violation at  $r = R_1$  with margin  $\approx -4.5 \times 10^{-4}$  (geometric, of the same sign and magnitude as the shift-free S-shell value), and an outer-boundary DEC violation near  $r = R_2$  of order  $10^{-2}$  at the default  $v_0 = 0.1$  (kinematic, scaling approximately linearly with the shift velocity; see Sec. 9). For  $v_0 = 0.1$  the outer-boundary residue is the binding violation.
- Maximum shift:  $|\beta^x|_{\max} = 0.00714$ .
- ADM mass:  $M = 3.12$ , Hawking–Ellis Type I throughout.

The inner-boundary DEC residue is a generic feature of smooth-transition shells: the rapid change in matter profiles at the shell–vacuum interface generates curvature contributions that the multi-observer certification detects as DEC-negative for certain timelike observers. The effect is absent in the deep interior where profiles vary slowly. We vary the velocity parameter down to the formally static limit,  $v_0 \in \{0, 0.01, 0.05, 0.1, 0.2\}$  at fixed source amplitude. The  $r = R_1$  boundary DEC margin changes by only  $\sim 3\%$  across this range ( $-4.42$  to  $-4.55 \times 10^{-4}$ ), and the  $v_0 = 0$  and  $v_0 = 0.01$  endpoints agree to four significant figures. The inner-boundary failure is therefore geometric in origin, driven by the spatial-curvature contribution of the smooth transition, rather than kinematic. The outer-boundary residue, by contrast, scales linearly with  $v_0$  and vanishes in the static limit, which identifies it as shift-induced. The T-shell achieves interior EC compliance but fails at both boundaries; to assess whether this is tunable or generic, we scan the parameter space over compactness and thickness.

## 8 Parameter scan

We scan the T-shell parameters over compactness  $\mathcal{C} = M/R_2 \in [0.01, 0.20]$  and thickness ratio  $\Delta R/R_2 \in [0.3, 0.8]$  on a  $20 \times 15$  grid ( $R_2 = 20$  fixed). At each grid point we set the density from the target compactness and evaluate the default Bernstein profiles with  $v_0 = 0.1$ .

**Table 1.** Admissibility summary for the three constructions with an explicit matter model (Fuchs, S-shell, T-shell). Fuchs is metric-first in construction but is evaluated against its prescribed canonical Gaussian-smoothed source, not the pre-smoothing analytic intermediate. Criterion B reports both constraint residuals, the Hamiltonian  $\epsilon_{\mathcal{H}}$  and the momentum  $\epsilon_{\mathcal{M}}$ ; note the T-shell  $\epsilon_{\mathcal{M}} \approx 4 \times 10^{-4}$  is the same order as its inner-boundary DEC margin. “D int.” denotes interior probes with 2% boundary offsets ( $r \in [10.2, 19.8]$ ); “D trans.” identifies the binding boundary-failure location. “Mass” is the integrated source mass; for the compact-support S- and T-shells the exterior is exactly Schwarzschild at  $r = R_2$ , so this equals the ADM mass at spatial infinity, whereas the Gaussian-smoothed Fuchs tail extends slightly beyond  $R_2$  and the matching is approximate (bulk-transition ADM diagnostics are evaluated under criterion E). Verdict “Partial”  $\equiv$  criteria A–C and E satisfied but D (energy conditions) fails at the transition; no construction meets the full standard.

Criterion	Fuchs	S-shell	T-shell
A. Regularity	✓	✓	✓
B. max $\epsilon_{\mathcal{H}}$	$3 \times 10^{-8}$	$2 \times 10^{-6}$	$3 \times 10^{-6}$
B. max $\epsilon_{\mathcal{M}}$	$4 \times 10^{-4}$	$\equiv 0$	$4 \times 10^{-4}$
C. Matter	aniso.	iso., static	iso., tilted
D int.	pass	pass	pass
D trans.	tail $r > R_2$	$r = R_1$	$r = R_1, R_2$ (outer binds)
E. Mass	+2.98	+3.09	+3.12
Verdict	Partial	Partial	Partial

Our principal result is negative: *we find no configuration in the surveyed range that achieves strict frame-independent EC admissibility across the full shell domain  $[R_1, R_2]$* . Figure 4(d) colors each grid point by the signed worst frame-independent EC margin (the gauge-dependent transport proxy  $\max |\beta^x|$  is discussed in Sec. 9). All 300 grid points show at least one DEC-negative probe, concentrated at the shell boundaries.

A companion  $20 \times 15$  scan of the shift-free S-shell on the same grid (Fig. 3(d)) again finds 0/300 EC-feasible configurations, with worst-margin magnitudes spanning  $|\text{margin}| \in [2 \times 10^{-10}, 2.7 \times 10^{-4}]$ . At the high- $\mathcal{C}$  corner ( $\mathcal{C} = 0.20, \Delta R/R_2 = 0.8$ ) the T-shell worst margin  $\approx -2.78 \times 10^{-2}$  is more than two decades worse than the S-shell value  $\approx -6.8 \times 10^{-5}$  at the same grid point. The S-shell’s globally worst *sweep* margin  $-2.7 \times 10^{-4}$  occurs in the thin-shell regime near  $(\mathcal{C}, \Delta R/R_2) \approx (0.20, 0.41)$ ; the sweep certifies each point on a coarser radial grid (15 probes,  $n_{\text{starts}} = 8$ ) than the dedicated single-metric runs, so it slightly under-resolves the boundary peak: the default configuration, probed densely, resolves a larger inner-boundary value ( $-4.5 \times 10^{-4}$ ; Sec. 6), and the sweep magnitudes are correspondingly conservative. Either way the S-shell stays two decades smaller in magnitude than the T-shell at its own globally worst point. The constraint-derived shift that gives the T-shell its transport utility therefore costs the construction  $\sim 10^2$ – $10^3 \times$  in frame-independent EC margin relative to the shift-free baseline, depending on the comparison point.

Grid convergence is checked at two representative grid points,  $(\mathcal{C}, \Delta R/R_2) = (0.01, 0.336)$  and  $(0.20, 0.80)$ , over  $n_{\text{grid}} \in \{256, 512, 1024\}$  (Table 2): the *sign* of the worst margin is grid-stable (negative at every resolution). The *magnitudes* vary across the grid by orders of magnitude, from  $|\text{margin}| \sim 10^{-4}$  in the low-compactness corner ( $\mathcal{C} \lesssim 0.03, \Delta R/R_2 \lesssim 0.35$ ) to  $|\text{margin}| \sim 10^{-2}$  at high compactness ( $\mathcal{C} \gtrsim 0.15$ ). The extreme  $10^{-10}$ -scale values seen at intermediate resolutions are optimizer-restart artifacts, not indicators of near-admissibility, as we confirm by re-evaluation at  $n_{\text{grid}} = 1024$ .

This gradient quantifies how tightly the EC constraint binds: source-first shells with moderate compactness are limited not by the matter model or by constraint satisfaction but by the Lorentz-invariant DEC margin at the transition boundaries. The bulk violations at high  $\mathcal{C}$  share the algebraic Type IV character of the Fuchs smoothing tail (Sec. 4), which points to a common geometric origin in the curvature contributions of the smooth source–vacuum transition.

**Robustness of the boundary violation.** Because the binding margin and the constraint residual both peak at the transition, we checked that the violation is not a numerical artifact. At both binding configurations the sign of the worst DEC margin stays negative across grid resolutions  $n_{\text{grid}} \in \{256, 512, 1024\}$ , optimizer restarts  $n_{\text{starts}} \in \{4, 8, 16, 32\}$  (saturating by  $n_{\text{starts}} = 8$ ), and a change of source-profile family ( $\mathcal{C}^2$  smoothstep versus parabolic compact support), eighteen settings in all. The constraint residual and the margin magnitude are in fact *anticorrelated* (Pearson  $\approx -0.66$ ): switching to a smoother (parabolic) source profile lowers the constraint residual yet drives the worst DEC margin *more* negative, which confirms that the violation is a geometric feature of the smooth transition rather than a residue of finite constraint error. A complementary angular check at the inner boundary, which samples the worst

$\min(\text{NEC}, \text{WEC}, \text{DEC})$  over the full 2-sphere of spatial directions and observer boosts rather than along the symmetry axis alone, returns the axial value ( $-4.45 \times 10^{-4}$  at  $r = R_1$ ) as the global worst over the sphere to within 0.02%, so for this  $x$ -axisymmetric geometry the binding direction lies on the symmetry axis that the radial probe follows.

Table 3 consolidates the five-criterion evaluation for all eight proposals. None passes the full standard. The Fuchs shell is the only *metric-first* proposal with positive ADM mass, but it fails criterion D in the smoothing-tail transition. The source-first S-shell and T-shell achieve the best constraint satisfaction and positive interior EC margins, but retain inner-boundary DEC violations. The Natário-class metrics (Alcubierre, Natário, Van den Broeck, Rodal, Lentz) lack both a source model and positive ADM mass.

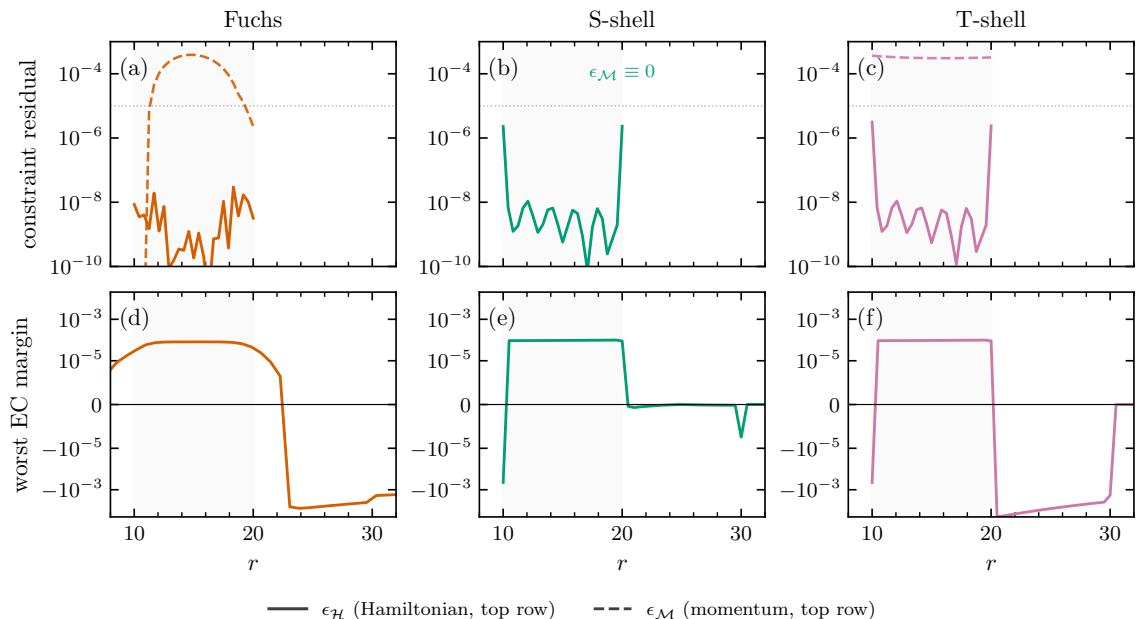


**Figure 2.** All three constructions pass the interior energy conditions; EC failure is localized to the boundary in every case. Top row: normalized constraint residuals (Eq. 10), evaluated against the prescribed Eulerian source, vs. radial coordinate (log scale) – the Hamiltonian  $\epsilon_{\mathcal{H}}$  (solid) and momentum  $\epsilon_{\mathcal{M}}$  (dashed); dotted line:  $\epsilon_{\mathcal{H}} = 10^{-5}$  reference. The Hamiltonian residual sits at  $\sim 10^{-6}$  (S/T-shells) and  $\sim 10^{-8}$  (Fuchs); the momentum residual is  $\equiv 0$  for the shift-free S-shell but reaches  $\sim 4 \times 10^{-4}$  for the Fuchs and T-shell shells, the same order as the inner-boundary DEC margin – so not every residual sits far below the EC margins. Bottom row: worst frame-independent EC margin  $\min(\text{NEC}, \text{WEC}, \text{DEC})$  after multi-start BFGS ( $n_{\text{starts}} = 16$ ) over the timelike-observer family (symlog, signed; zero line: admissibility threshold), plotted for  $r \geq R_1$  (the T-shell inner vacuum carries a uniform-shift gauge artifact, excluded here as in Fig. 4). Failure locations: Fuchs in the smoothing tail  $r > R_2$ ; S/T-shells at the  $C^2$  shell junctions, with the T-shell also dipping at the outer boundary  $r \approx R_2$  (kinematic, from the shift). Shaded bands mark the shell region  $[R_1, R_2]$ .

**Table 2.** Grid-resolution robustness of the worst frame-independent EC margin at two representative T-shell grid points across  $n_{\text{grid}} \in \{256, 512, 1024\}$ . The result here is the *sign* stability (negative at every resolution), not magnitude convergence: the magnitude is non-monotone in  $n_{\text{grid}}$ , and the low- $\mathcal{C}$  row’s  $-5.1 \times 10^{-10}$  at  $n_{\text{grid}} = 512$  is an optimizer-restart outlier (the  $n_{\text{grid}} = 1024$  value,  $\sim 10^{-4}$ , is representative). The high- $\mathcal{C}$  row is stable at  $\sim 10^{-2}$  across resolutions.

$(\mathcal{C}, \Delta R/R_2)$	$n_{\text{grid}}=256$	$n_{\text{grid}}=512$	$n_{\text{grid}}=1024$	sign
(0.01, 0.336)	$-3.5 \times 10^{-4}$	$-5.1 \times 10^{-10}$	$-1.8 \times 10^{-4}$	–
(0.20, 0.800)	$-6.7 \times 10^{-3}$	$-2.8 \times 10^{-2}$	$-2.4 \times 10^{-2}$	–

## 9 Discussion

**Frame-independent vs. Eulerian analysis.** Our Fuchs verification pins down where the Santiago–Schuster–Visser observer-dependence mechanism [16] bites for a concrete construction. For the Gaussian-smoothed Fuchs metric the bulk shell interior  $[R_1, R_2]$  is genuinely EC-compliant under both Eulerian and multi-observer certification (0/13 interior violations, all Hawking–Ellis Type I). The multi-observer search detects violations in the smoothing tails ( $r > R_2$ ), where the iterative kernel deposits a residual matter halo that is locally Type IV: 22 of 25 exterior probes

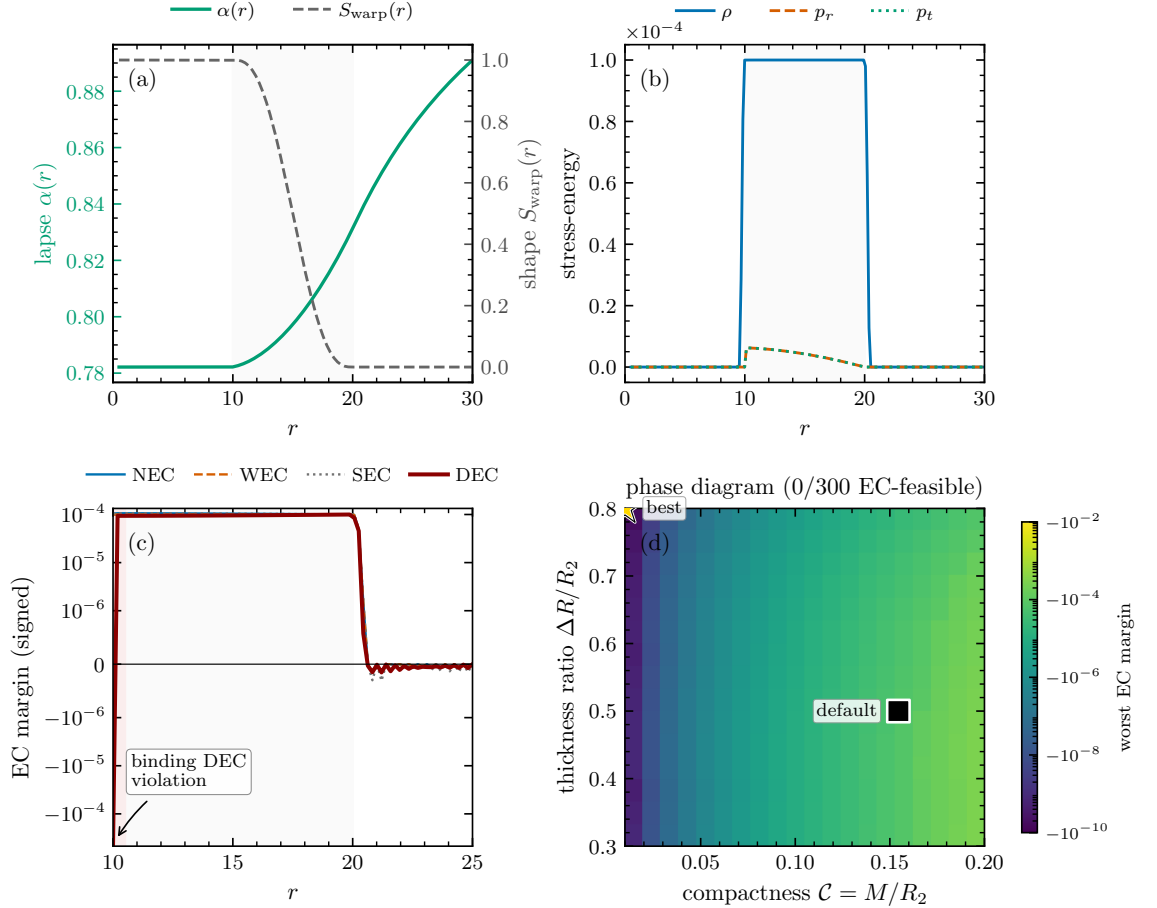


**Figure 3.** S-shell (Class I) default configuration ( $R_1 = 10$ ,  $R_2 = 20$ ,  $\rho_0 = 10^{-4}$ ,  $\beta^i \equiv 0$ ). (a) Lapse  $\alpha(r)$  (left axis) and warp shape indicator  $S_{\text{warp}}(r)$  (right axis; the dimensionless  $C^2$  shape function, 1 in the interior and 0 in the exterior); the shift vanishes by construction. (b) Isotropic source profiles  $\rho(r)$ ,  $p_r(r) = p_t(r)$ . (c) Pointwise NEC/WEC/DEC/SEC margins vs.  $r$  (symlog; multi-start BFGS,  $n_{\text{starts}} = 16$ ). The binding constraint is the boundary DEC violation at  $r = R_1$  (margin  $\approx -4.5 \times 10^{-4}$ ) from the  $C^2$  smoothstep junction; the inner vacuum region  $r < R_1$  is omitted. (d)  $(C, \Delta R/R_2)$  heatmap from the  $20 \times 15$  scan ( $R_2 = 20$  fixed; symlog, negative-only). Gold star: scan best-margin point. Black square: default parameters used in (a)–(c). Shaded band in (a)–(c): shell region  $[R_1, R_2]$ .

**Table 3.** Five-criterion admissibility comparison across eight warp-drive proposals, spanning the four construction classes (Alcubierre–Natário, conformal Van den Broeck, metric-first Fuchs/Lentz/Rodal, and source-first S/T-shells). Symbols:  $\checkmark$  pass,  $\times$  fail,  $—$  not applicable; “tauto”: tautologically satisfied for metric-first constructions where  $T_{ab} \equiv G_{ab}/8\pi$ ; “int”/“bnd”: interior ( $r \in [10.2, 19.8]$ ) and inner-boundary ( $r = R_1$ ) probes. EC margins are evaluated under multi-start BFGS certification ( $n_{\text{starts}} = 16$ ). The Fuchs column refers to the canonical Gaussian-smoothed shell (Sec. 4), not the pre-smoothing analytic intermediate. Alcubierre, Natário, and Van den Broeck are verified at  $v_s = 0.1$ ,  $R = 20$ ,  $\sigma = 2$ . “Total mass” reports  $M_{\text{ADM}}$  for Natário-class constructions (zero by  $1/r$ -falloff absence) and the integrated source mass matched to the Schwarzschild exterior at  $r = R_2$  for the source-prescribed shells; both definitions coincide when a Schwarzschild matching exists. This table reports pass/fail only; the Criterion-B residual values and the transition-failure locations for Fuchs, S-shell, and T-shell are listed in Table 1 (verdict “Partial” defined there).

Criterion	Alcubierre	Natário	VdB	Lentz	Rodal	Fuchs	S-shell	T-shell
A. Regularity	$\checkmark$	$\checkmark$	$\checkmark$	$\checkmark$	$\checkmark$	$\checkmark$	$\checkmark$	$\checkmark$
B. Constraints	tauto	tauto	tauto	tauto	tauto	$\checkmark$	$\checkmark$	$\checkmark$
C. Matter model	$—$	$—$	$—$	$—$	$—$	$\checkmark$	$\checkmark$	$\checkmark$
D. EC interior	$\times$	$\times$	$\times$	$\times$ [17]	$\times$	$\checkmark$ (0/13)	$\checkmark$	$\checkmark$
D. EC transition	$\times$	$\times$	$\times$	$\times$ [17]	$\times$	$\times$	$\times$	$\times$
E. Total mass	0	0	0	0	0	+2.98	+3.09	+3.12
Verdict	Fail	Fail	Fail	Fail	Fail	Partial	Partial	Partial

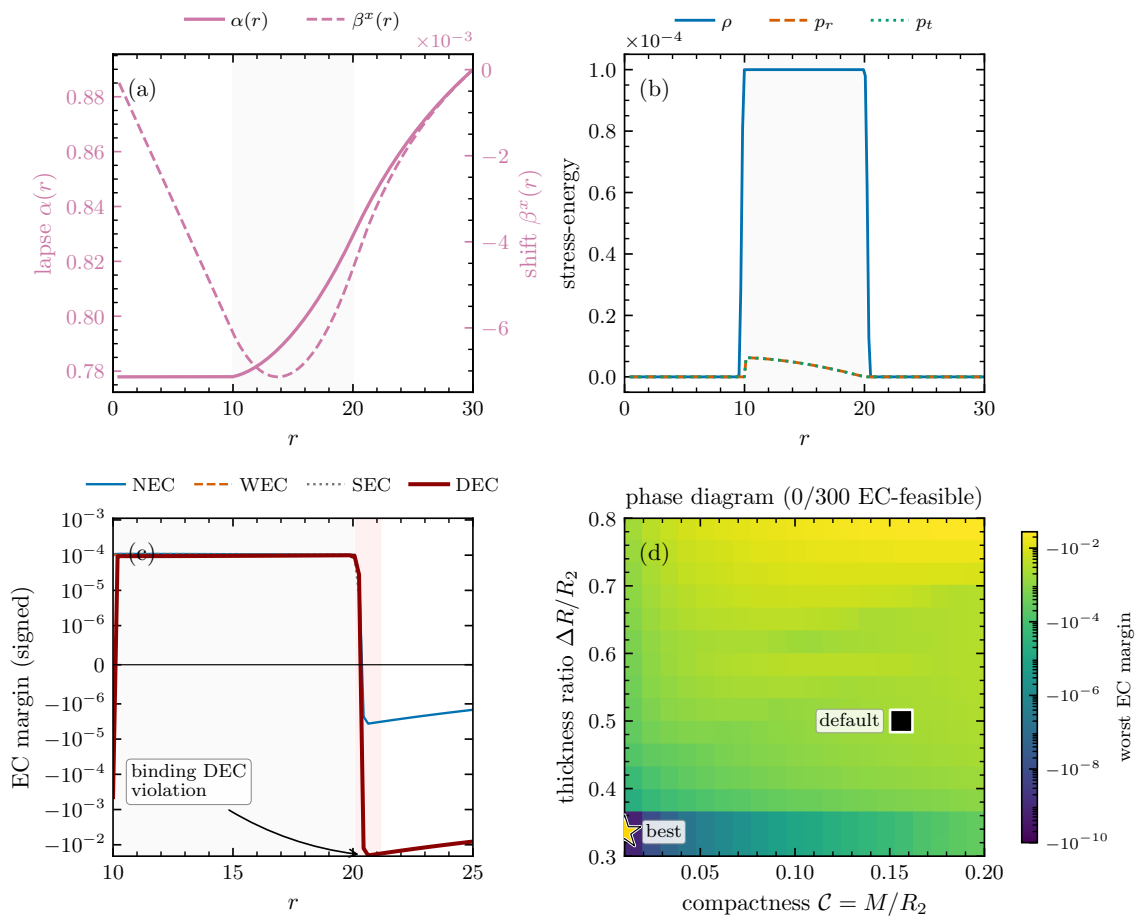


**Figure 4.** T-shell (Class II) default configuration ( $R_1 = 10$ ,  $R_2 = 20$ ,  $\rho_0 = 10^{-4}$ ,  $v_0 = 0.1$ ). (a) Lapse  $\alpha(r)$  (left axis) and constraint-derived shift  $\beta^x(r)$  (right axis); the shift is a solution of the momentum constraint, not a free design choice. (b) Isotropic source profiles  $\rho(r)$ ,  $p_r(r) = p_t(r)$ . (c) Pointwise NEC/WEC/DEC/SEC margins (symlog; multi-start BFGS,  $n_{\text{starts}} = 16$ ) in the shell and near exterior. The binding violation is a boundary DEC failure near  $r = R_2$  ( $\sim 10^{-2}$  margin) from the  $C^2$  smoothstep on the shift. The inner vacuum region  $r < R_1$  carries a uniform-shift gauge artifact (discussed in Sec. 9); the EC verdict is gauge-invariant in the shell and near exterior shown here. (d)  $(C, \Delta R/R_2)$  heatmap from the  $20 \times 15$  scan. Markers as in Fig. 3.

**Table 4.** Criterion-E global/invariant diagnostics for all eight constructions, evaluated uniformly: ADM mass  $M_{\text{ADM}}$  (a surface integral at  $r = R_2$  that equals the ADM mass at infinity because the exterior is exactly Schwarzschild for the source-prescribed shells; zero by  $1/r$ -falloff absence for the Natário-class metrics), cavity tidal acceleration  $A_{\text{geo}}$ , and the null round-trip asymmetry  $\delta\tau$  as the representative invariant transport observable. All quantities are in geometric units ( $G = c = 1$ ). The E verdict is set by positive ADM mass (the binding sub-criterion); the cavity tidal accelerations  $A_{\text{geo}}$  all fall below the passenger-safety threshold of criterion E (Sec. 2). “ $\sim 0$ ” denotes a value vanishing by symmetry or below the numerical resolution ( $\lesssim 10^{-12}$ ):  $\delta\tau$  vanishes for the shift-free S-shell and for the flat-interior Lentz/Van den Broeck rays, whereas a nonzero  $\delta\tau$  certifies genuine, gauge-invariant transport.

Construction	$M_{\text{ADM}}$	$A_{\text{geo}}$ (cavity)	$\delta\tau$	E
Alcubierre	0	$1.2 \times 10^{-3}$	-2.6	×
Natário	0	$1.8 \times 10^{-7}$	-41	×
Van den Broeck	0	$\sim 0$	$\sim 0$	×
Lentz	0	$\sim 0$	$\sim 0$	×
Rodal	0	$2.2 \times 10^{-11}$	-40	×
Fuchs	+2.98	$1.3 \times 10^{-8}$	-1.8	✓
S-shell	+3.09	$\sim 0$	$\sim 0$	✓
T-shell	+3.12	$6.2 \times 10^{-7}$	-0.80	✓

violate WEC/DEC under multi-start BFGS, with the worst margin reaching  $-7.9 \times 10^{-3}$  at  $r \approx 23.9$ . An Eulerian-only analysis of these exterior points misses the violations because the Type IV regions permit positive Eulerian-frame margins while no Lorentz observer makes the stress-energy globally positive.

**Constraint satisfaction and its separation from the EC verdict.** Evaluated against the prescribed Eulerian source, all three shells satisfy the Einstein constraints to solver precision:  $\epsilon_{\mathcal{H}} \approx 3 \times 10^{-8}$  for the canonical Fuchs metric and  $\approx 2-3 \times 10^{-6}$  for the S/T-shells, with  $\epsilon_{\mathcal{M}} \lesssim 4 \times 10^{-4}$ . (The matter magnitude  $16\pi E \sim 5 \times 10^{-3}$ , returned by a vacuum residual that omits the source term, should not be mistaken for the constraint residual.) The Hamiltonian residual  $\epsilon_{\mathcal{H}}$  lies well below the energy-condition margins: roughly one-and-a-half orders for the S/T-shells and three-and-a-half for Fuchs against the  $\sim 10^{-4}$  interior margins, and further below the larger boundary violations. The momentum residual  $\epsilon_{\mathcal{M}} \approx 4 \times 10^{-4}$ , however, is comparable to the inner-boundary DEC margin; for the inner boundary the case against a numerical artifact therefore rests not on residual magnitude but on the robustness analysis of Sec. 8, where reducing the residual through a smoother source prescription leaves the violation in place and, if anything, deepens it (residual and margin are anticorrelated, Pearson  $\approx -0.66$ ). The binding outer-boundary violation ( $\sim 10^{-2}$ ) is in any case more than an order of magnitude above both residuals. For the source-first shells the residual is the pure discretization error of a TOV/momentum-constraint solver acting on prescribed profiles; for the metric-first Fuchs shell it is the post-smoothing remainder of a procedure that began with constant-density profiles, and its *full* stress still carries an  $\mathcal{O}(0.4)$  source mismatch (Sec. 4) that the source-first shells avoid in their interior.

**Transition-zone EC failure as a generic phenomenon.** The central finding across our verification is that every smooth source–vacuum transition we examined fails the multi-observer DEC, but the *location* of the failure depends on the construction: (i) for the Gaussian-smoothed Fuchs, the failure is in the smoothing tail  $r > R_2$ , where 22 of 25 probes are Type IV with margins  $\sim 10^{-3}$ ; (ii) for the S/T-shells with strict compact support in  $[R_1, R_2]$  and a  $C^2$  smoothstep junction, the failure is at the inner boundary  $r = R_1$  with margin  $\sim -4.5 \times 10^{-4}$ ; (iii) none of the 600 grid points (300 T-shell + 300 S-shell, Figs. 3(d) and 4(d)) achieves strict frame-independent EC admissibility. Alternative transition profiles ( $C^k$  with  $k > 2$ , or thin-shell limits via Israel junctions [9, 23]) are candidate strategies for moving the failure location, but no construction we are aware of removes it entirely.

**Prescription residues and the scaling toward EC feasibility.** The transition-zone failures are residues of the chosen  $C^2$  smoothstep ansatz on  $\rho$ ,  $p$ , and  $v_x$ , and they separate into two contributions (Fig. 6). First, the T-shell outer-boundary DEC margin scales *linearly* with the shift velocity,  $|\delta_{\text{DEC}}| \approx 0.2 v_0$  for  $v_0 \gtrsim 3 \times 10^{-3}$ , and saturates at the  $v_0$ -independent S-shell inner-boundary floor below that crossover. This residue is kinematic, originating in the shift-gradient stress  $\partial\beta^x$  at the outer transition. Second, replacing the  $C^2$  smoothstep density with a polynomial compact-support profile (parabolic, Bernstein) reduces the geometric inner-boundary floor by a factor of 2 to 6 at fixed  $v_0$ , which indicates that the floor reflects the regularity class of the source prescription. Both behaviors are quantitatively consistent with the iterative-smoothing residues of Fuchs *et al.* [2], who reduce their *Eulerian-frame* residues to a  $\sim 10^{-6}$  floor through four passes of moving-average filtering on  $\rho$  and  $p$ ; this Eulerian floor is distinct from, and does not preclude, the frame-independent tail margin ( $\sim -8 \times 10^{-3}$ ) we report in Sec. 4. We do not claim a fully EC-feasible classical construction here; the data are consistent with prescription-dependent residues that can be suppressed by combining (a) smaller  $v_0$ , (b) smoother analytic source profiles, and (c) iterative source smoothing in the style of [2]. The present data do not establish that the residues can be driven to zero in the continuum or optimized-profile limit; whether such a limit admits a fully EC-feasible classical state, or instead requires a quantum field-theoretic treatment respecting ANEC and the relevant quantum inequalities [5, 6, 31], remains open.

**Gauge dependence of transport.** The coordinate shift  $\beta^x$  is not a gauge-invariant observable. The maximum values in our scan ( $\sim 0.003$  at high compactness) represent tiny perturbations of Minkowski spacetime and should not be read as physically meaningful warp effects. Invariant transport diagnostics (the null round-trip asymmetry  $\delta\tau$  following Fuchs *et al.* Section 5.1 [2], the geodesic deviation  $A_{\text{geo}}$ , and the blueshift hazard  $\mathcal{B}$ ) are implemented in WARPAX and evaluated independently. For the T-shell at default parameters ( $R_1=10$ ,  $R_2=20$ ,  $\rho_0=10^{-4}$ ,  $v_0=0.1$ ) we obtain  $\delta\tau \approx -0.795$  (geometric units) along a null round-trip from  $x = -25$  to  $x = +25$ ; raising  $v_0 \rightarrow 0.2$

yields  $\delta\tau \approx -1.67$  (a factor of  $\sim 2.1$  per  $v_0$  doubling, near-linear in the bubble velocity with a  $\sim 5\%$  sub-linear correction), which confirms that the shift produces a gauge-invariant transport signal rather than a coordinate artifact. The Fuchs light-ray experiment likewise yields a non-zero  $\delta\tau$  for the warp shell and  $\delta\tau = 0$  for a static shell. Future work should parameterize the design space by these invariant observables.

**An exploratory averaged null-ray diagnostic.** The pointwise DEC failures at the smooth shell boundaries do not, by themselves, imply averaged-EC failures. As an exploratory check we compute the line integral  $\int T_{ab}k^ak^b d\lambda$  along an off-axis coordinate null ray (Fig. 5;  $y = 10^{-3}$  to avoid the on-axis coordinate-chart singularity in Natário-class shape functions). For the three source-prescribed shells the ray stays genuinely null along the path ( $|g_{ab}k^ak^b| < 10^{-6}$ ), so the integrand measures the null energy, and the integral is positive: Fuchs  $\approx +5.0 \times 10^{-4}$ , S-shell  $\approx +6.5 \times 10^{-4}$ , T-shell  $\approx +3.8 \times 10^{-3}$ . The high-compactness T-shell at the binding corner ( $\mathcal{C} = 0.20$ ,  $\Delta R/R_2 = 0.80$ , worst pointwise margin  $-2.78 \times 10^{-2}$ ) gives a positive line integral  $\approx +6.7 \times 10^{-3}$ , so the diagnostic stays positive across the surveyed range. The Fuchs value varies by less than 0.3% over an off-axis scan  $y \in \{10^{-3}, \dots, 1\}$ . We do not report a value for the Alcubierre baseline: the strong shift bubble drives the same ray off the null cone ( $\max |g_{ab}k^ak^b| \sim 0.23$ ), so  $T_{ab}k^ak^b$  along that ray no longer measures the NEC; the relevant statement there is the Pfenning–Ford result [5].<sup>1</sup> We stress that a single ray is not a proof of ANEC: the relevant test is a full geodesic-integrated average over a representative family of null geodesics, which we leave to future work [32]. With that caveat, the positive sign is qualitatively in keeping with the semiclassical expectation that averaged conditions can survive where pointwise ones fail (the Flanagan–Wald argument [7]; the achronal ANEC has a rigorous QFT proof by Faulkner *et al.* [31], established for Minkowski-space quantum fields rather than the curved warp-shell geometry; see also the modern energy-condition review [10]): the pointwise boundary failures of Secs. 4–7 need not appear in this averaged diagnostic, even at the binding pointwise-failure corner.

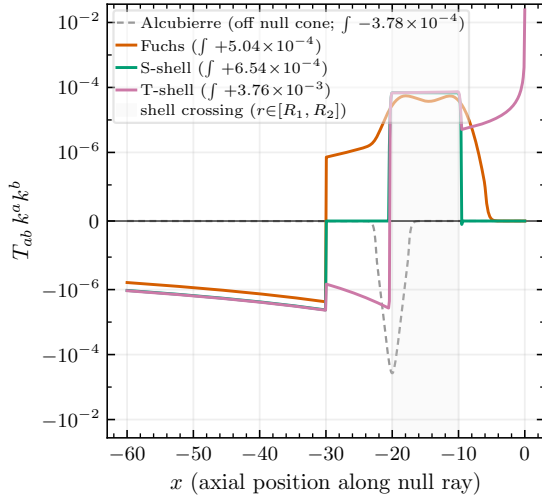


**Figure 5.** Null-energy contraction  $T_{ab}k^ak^b$  along an off-axis coordinate null ray ( $y = 10^{-3}$ ) for each construction; shaded band: shell crossing  $r \in [R_1, R_2]$ . The legend reports the coordinate-ray line integral  $\int T_{ab}k^ak^b d\lambda$  ( $\lambda$  the coordinate parameter, not an affine geodesic parameter), positive for every source-prescribed shell. This is an exploratory diagnostic, not an affinely-parameterized ANEC test over complete null geodesics (Sec. 9; Ref. [5]). Alcubierre (grey, dashed) is context only: its ray drifts off the null cone ( $\max |g_{ab}k^ak^b| \sim 0.23$ ), so its contraction does not measure the NEC.

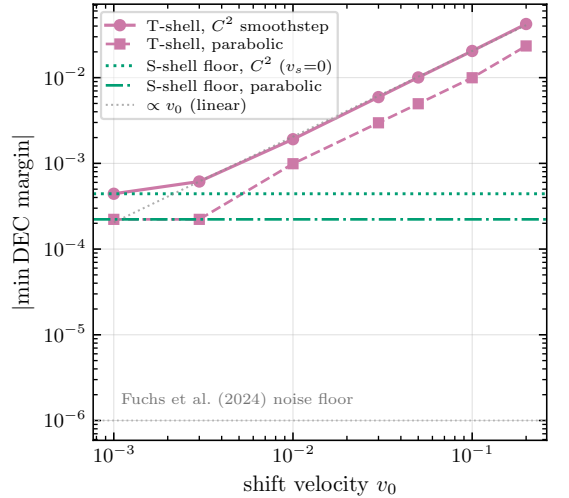


**Figure 6.**  $|\text{min DEC margin}|$  for the T-shell vs. shift velocity  $v_0$ , for  $C^2$ -smoothstep (circles) and parabolic (squares) source profiles; horizontal lines mark the corresponding  $v_0=0$  S-shell inner-boundary floors (read off the log  $y$ -axis). The violation scales linearly with  $v_0$  above a  $v_0$ -independent geometric floor, saturating onto it for  $v_0 \lesssim 3 \times 10^{-3}$ ; the parabolic profile lowers both the envelope and the floor by  $\sim 2$ . The two knobs identify the boundary DEC violation as a prescription residue – a kinematic part (linear in  $v_0$ ) and a geometric floor set by the profile regularity. The Fuchs *et al.* [2]  $\sim 10^{-6}$  smoothing floor is shown for reference.

<sup>1</sup>The path is a coordinate null ray, not a metric geodesic, and ANEC magnitudes carry a scale ambiguity under  $k^a \rightarrow \lambda k^a$ , so only the *sign* of the integral is invariant. A supplementary geodesic cross-check (WARPAX adaptive Runge–Kutta,  $\text{rtol} = \text{atol} = 10^{-10}$ ) preserves  $g_{ab}k^ak^b = 0$  to better than  $3 \times 10^{-6}$  along the path for the source-prescribed shells and yields sign-consistent integrals.

**Outlook across proposals.** Across the six metric-first proposals, no existing subluminal construction satisfies the full standard. The Natário-class metrics (Rodal, Lentz) have a simpler algebraic structure but lack both a source model and positive ADM mass, the two features the Barzegar–Buchert–Vigneron analysis [18, 19] identifies as essential. The Fuchs shell has both but fails the multi-observer EC certification. A natural next step is to combine the source-first methodology of the T-shell with the ADM-mass engineering of the Fuchs approach, and to extend the source-first treatment to the Fell–Heisenberg [33] and membrane [34] models. Two recent results bear on this outlook. The constraint-derived T-shell shift is obtained from the momentum constraint for a tilted matter flow rather than postulated, in the same source-respecting spirit as the Rodal [3] and de Sitter Garattini–Zatrimaylov [15] constructions that reduce their peak NEC/WEC stress; yet our results indicate that such bulk improvements do not cure the transition-boundary DEC failure. The thin-shell membrane route of Huey [34], in which an Israel–Darmois surface layer [23] carries the energy-condition burden, is complementary to our thick-shell ( $R_2 - R_1 = 10$ ) treatment: the boundary deficit we localize is what a thin-shell junction repackages as surface stress, so comparing the two is a direct test of whether the failure is removable or merely relocated. The negative-energy excursions we find are in any case classical; quantum energy inequalities [6, 32] bound their magnitude and fix the scale below which a semiclassical treatment must replace the classical one.

**Limitations.** The analysis is restricted to subluminal, static initial data on a single time slice at fixed  $v_0 = 0.1$  with default Bernstein profiles; the EC verdicts are invariant under joint rescaling of  $(R_1, R_2, M_{\text{ADM}})$  at fixed  $(\mathcal{C}, \Delta R/R_2)$ , so  $R_2 = 20$  is representative without loss of generality. Time evolution, dynamical stability, full averaged-EC integrals over geodesic families, and direct quantum-inequality comparisons [5–7, 10] are out of scope. The pointwise NEC/DEC violations at the smooth shell boundaries may or may not appear in averaged integrals along arbitrary null geodesics; the single-ray positivity reported here is a diagnostic, not a proof of ANEC. The source-first shells are built from the spherically reduced (static) constraint system; we have verified that the neglected extrinsic-curvature terms are negligible (Sec. 3) and that the boundary verdict is unchanged under full 2-sphere angular sampling (Sec. 8), but a fully three-dimensional,  $K$ -coupled solve for strongly tilted ( $v_0 \rightarrow 1$ ) flows remains for future work. Because that reduction treats the angle-dependent source on-axis (Sec. 3), genuinely angular (non-spherical) source profiles are likewise unexplored and could, in principle, shift the  $\sim 10^{-4}$  geometric boundary floor that the purely radial prescriptions produce. Alternative profile shapes or matter-model classes (scalar, vector, electromagnetic, elastic shell) could reveal pockets of EC feasibility we have not captured.

## 10 Conclusions

We have proposed a five-criterion admissibility standard for subluminal positive-energy warp shells and applied it to six existing proposals and two new source-first constructions. Across the constructions examined, none satisfies the full standard, and the binding constraint is not energy-condition satisfaction in the bulk interior: both the metric-first Fuchs shell and the source-first S/T-shells achieve positive NEC, WEC, and DEC margins deep inside. Rather, across the constructions and profiles surveyed, the limiting violations occur at the smooth source–vacuum transition. We interpret this as a prescription residue that separates into a kinematic contribution (the shift velocity) and a geometric one (the source-profile regularity); the present data do not establish that the residue can be driven to zero in the continuum limit, but neither do they constitute a no-go theorem. For the Gaussian-smoothed Fuchs construction the failure occurs in the smoothing tail ( $r > R_2$ ), where 22 of 25 exterior probes are Hawking–Ellis Type IV with margins  $\sim 10^{-3}$ . For the source-first S/T-shells the inner-boundary failure occurs at  $r = R_1$  with margin  $\sim -4.5 \times 10^{-4}$ , and the T-shell also develops a shift-induced outer-boundary residue near  $r = R_2$  that scales linearly with  $v_0$ .

The independent recurrence of the inner-boundary residue across the shift-free and tilted classes supports the interpretation that this transition-zone failure is geometric within this family of source prescriptions: it is independent of bubble velocity (the velocity variation confirms that it persists in the formally static  $v_0 = 0$  limit) and is not removed by the choice of shift. Source-profile regularity and iterative smoothing reduce the floor magnitude without yet eliminating it.

The source-inconsistency problem identified by Barzegar, Buchert, and Vigneron is instantiated concretely in the  $\sim 640\times$  pointwise divergence between the metric-derived and prescribed stresses in the pre-smoothing Fuchs intermediate. Our  $20 \times 15$  scan (300 T-shell + 300 S-shell configurations) extends this to the surveyed source-first parameter range: 0 of 600 configurations achieve strict frame-independent EC admissibility across the full domain  $[R_1, R_2]$ , consistent with

the Lobo–Visser obstruction [8] across this surveyed family under the stricter multi-observer standard. The worst-margin magnitude spans eight orders of magnitude across the surveyed grid before saturating against the source–vacuum transition floor.

At the averaged level the picture is more favorable, with the caveat that our averaged diagnostic is a single coordinate ray rather than a geodesic average. The null-ray energy line integral is positive along a representative off-axis ray for all three source-prescribed constructions (Fuchs, S-shell, T-shell), and stays positive at the high-compactness corner where the pointwise margin is most negative; we recall the Pfenning–Ford result for the Alcubierre baseline at the QFT level rather than reproducing it along a coordinate ray. Pointwise EC failures localized to thin transition layers therefore need not appear in this diagnostic. This pattern (pointwise classical-EC failures alongside positive null-ray integrals for every source-prescribed shell) is qualitatively in keeping with the semiclassical picture in which an achronal averaged null energy condition is the load-bearing constraint that survives renormalization (proved for Minkowski-space quantum fields by Faulkner *et al.* [31]), with quantum energy inequalities [5, 6, 10, 32] bounding the admissible negative-energy excursions. A full geodesic-integrated ANEC over a representative family of null geodesics is the natural test of this picture.

Alternative transition profiles ( $C^k$  with  $k > 2$ ), thin-shell limits via Israel junctions [23], and matter models beyond anisotropic fluids are candidates for relocating or removing the boundary failure. Time evolution and dynamical stability lie beyond the present static-data scope. The source-first methodology developed here offers a route to source consistency that complements the metric-first conventions dominant in the literature, and future warp-shell proposals may benefit from being designed and reported against an explicit admissibility standard of this kind.

## A Reduction of the momentum constraint to the shift equation

For the T-shell we prescribe the matter and obtain the shift from the momentum constraint rather than postulating it; we record the reduction used in Sec. 3.2. The spatial metric and lapse are  $\gamma_{ij} = \delta_{ij} + (e^{2\Lambda(r)} - 1)\hat{r}_i\hat{r}_j$  and  $\alpha = e^{\Phi(r)}$ , with the shift along a fixed Cartesian axis,  $\beta^i = \beta(r)\hat{x}^i$ . On the static slice ( $\partial_t\gamma_{ij} = 0$ ) the extrinsic curvature is

$$K_{ij} = \frac{1}{2\alpha}(D_i\beta_j + D_j\beta_i), \quad (11)$$

and the momentum constraint reads  $D_j(K^j_i - \delta^j_i K) = 8\pi S_i$  with  $S_i = \Gamma^2(\rho + p)v_i$  from Eq. (5). Substituting the ansatz, the trace and divergence of  $K_{ij}$  depend on  $r$  through  $\Phi, \Lambda$  and on the single radial profile  $\beta(r)$ . Contracting with  $\hat{x}^i$  and using the spherical symmetry of  $\gamma_{ij}$ , the radial projection of the constraint gives the linear second-order equation

$$\beta'' + A(r)\beta' + B(r)\beta = 8\pi\alpha S_x, \quad A = \frac{2}{r} + 2\Phi' - 2\Lambda', \quad B = -\frac{2}{r^2}, \quad (12)$$

with primes denoting  $d/dr$ . The  $2/r$  term in  $A$  is the flat-space radial weight,  $2\Phi' - 2\Lambda'$  carry the lapse and radial-potential gradients, and  $B = -2/r^2$  is the curl-free vector-Laplacian eigenvalue for the  $\ell = 1$  (dipole) angular pattern set by the single Cartesian direction of  $\beta^i$ . Equation (12) is solved as a tridiagonal boundary-value problem with  $\beta'(0) = 0$  (regularity) and  $\beta(r_{\max}) = 0$  (asymptotic flatness). We verify the reduction *a posteriori*: substituting the solved metric into the full covariant constraint  $\mathcal{M}_i = D_j(K^j_i - \delta^j_i K) - 8\pi S_i$ , evaluated by automatic differentiation independently of Eq. (12), leaves a normalized residual  $\epsilon_{\mathcal{M}} \approx 4 \times 10^{-4}$  across the shell (Sec. 7). Because  $\epsilon_{\mathcal{M}}$  is the norm  $\|\mathcal{M}_i\|$  over all three components, the angular components that the dipole ansatz does not solve directly are bounded by this residual rather than assumed to vanish, so the reduction reproduces the full three-dimensional momentum constraint to solver precision.

## Data availability

All computations, scans, and figures are reproducible from the WARPAX toolkit (<https://github.com/anindex/warpax>); see the README section “Reproducing results” for the script-by-script recipe.

## Acknowledgments

The author thanks the JAX, Equinox, and Optimistix development teams for the software infrastructure underlying this work. Computations used JAX [24] with Equinox [35], Optimistix [36], DiffraX [37], and interpax for cubic interpolation of the numerical shell profiles.

## References

- [1] Bobrick A and Martire G 2021 *Class. Quantum Grav.* **38** 105009 (*Preprint* [2102.06824](#))
- [2] Fuchs J, Helmerich C, Bobrick A, Sellers L, Melcher B and Martire G 2024 *Class. Quantum Grav.* **41** 095013 (*Preprint* [2405.02709](#))
- [3] Rodal J 2026 *Gen. Relativ. Gravit.* **58** 1 (*Preprint* [2512.18008](#))
- [4] Garattini R and Zatrımaylov K 2024 *Phys. Lett. B* **856** 138910 (*Preprint* [2408.04495](#))
- [5] Pfenning M J and Ford L H 1997 *Class. Quantum Grav.* **14** 1743–1751 (*Preprint* [gr-qc/9702026](#))
- [6] Ford L H and Roman T A 1996 *Phys. Rev. D* **53** 5496–5507 (*Preprint* [gr-qc/9510071](#))
- [7] Flanagan E E and Wald R M 1996 *Phys. Rev. D* **54** 6233–6283 (*Preprint* [gr-qc/9602052](#))
- [8] Lobo F S N and Visser M 2004 *Class. Quantum Grav.* **21** 5871–5892 (*Preprint* [gr-qc/0406083](#))
- [9] Visser M 1995 *Lorentzian Wormholes: From Einstein to Hawking* (New York: AIP Press)
- [10] Kontou E A and Sanders K 2020 *Class. Quantum Grav.* **37** 193001 (*Preprint* [2003.01815](#))
- [11] Olum K D 1998 *Phys. Rev. Lett.* **81** 3567–3570 (*Preprint* [gr-qc/9805003](#))
- [12] Le A T 2026 Observer-robust energy condition verification for warp drive spacetimes arXiv:2602.18023 35 pp. (*Preprint* [2602.18023](#))
- [13] Hawking S W and Ellis G F R 1973 *The Large Scale Structure of Space-Time* (Cambridge University Press)
- [14] Lentz E W 2021 *Class. Quantum Grav.* **38** 075015 (*Preprint* [2006.07125](#))
- [15] Garattini R and Zatrımaylov K 2025 Positive-energy warp drive in a De Sitter universe (*Preprint* [2502.13153](#))
- [16] Santiago J, Schuster S and Visser M 2022 *Phys. Rev. D* **105** 064038 (*Preprint* [2105.03079](#))
- [17] Celmaster W and Rubin S 2025 Violations of the weak energy condition for Lentz warp drives (*Preprint* [2511.18251](#))
- [18] Barzegar H, Buchert T and Vigneron Q 2026 General formalism, classification, and demystification of the current warp-drive spacetimes (*Preprint* [2602.16495](#))
- [19] Buchert T and Frackowiak A 2026 *Universe* **12** 132 (*Preprint* [2605.03653](#))
- [20] Barzegar H and Buchert T 2025 *Universe* **11** 293 (*Preprint* [2407.00720](#))
- [21] Weickert J 1998 *Anisotropic Diffusion in Image Processing* (Stuttgart: Teubner-Verlag)
- [22] Getreuer P 2013 *Image Processing On Line* **3** 286–310
- [23] Israel W 1966 *Nuovo Cimento B* **44** 1–14 erratum *ibid.* **48**, 463 (1967)
- [24] Bradbury J, Frostig R, Hawkins P, Johnson M J, Leary C, Maclaurin D, Necula G, Paszke A, VanderPlas J, Wanderman-Milne S and Zhang Q 2018 JAX: composable transformations of Python+NumPy programs <https://github.com/jax-ml/jax>
- [25] Carroll S M 2004 *Spacetime and Geometry: An Introduction to General Relativity* (Addison-Wesley)
- [26] Rodal J 2026 Weakly birefringent screening disfavors fast Hawking–Ellis Type I warp drives via low-velocity cubic tilt scaling arXiv:2603.21352v2 (24 March 2026) (*Preprint* [2603.21352](#))
- [27] Helmerich C, Fuchs J, Bobrick A, Sellers L, Melcher B and Martire G 2024 *Class. Quantum Grav.* **41** 095009 (*Preprint* [2404.03095](#))
- [28] Alcubierre M 1994 *Class. Quantum Grav.* **11** L73–L77 (*Preprint* [gr-qc/0009013](#))

- [29] Natário J 2002 *Class. Quantum Grav.* **19** 1157–1166 (*Preprint* [gr-qc/0110086](#))
- [30] Van Den Broeck C 1999 *Class. Quantum Grav.* **16** 3973–3979 (*Preprint* [gr-qc/9905084](#))
- [31] Faulkner T, Leigh R G, Parrikar O and Wang H 2016 *J. High Energy Phys.* **2016** 038 (*Preprint* [1605.08072](#))
- [32] Kontou E A 2024 *Universe* **10** 291 (*Preprint* [2405.05963](#))
- [33] Fell S D B and Heisenberg L 2021 *Class. Quantum Grav.* **38** 155020 (*Preprint* [2104.06488](#))
- [34] Huey G 2024 *Class. Quantum Grav.* **41** 135007 (*Preprint* [2311.07193](#))
- [35] Kidger P and Garcia C 2021 Equinox: neural networks in JAX via callable PyTrees and filtered transformations (*Preprint* [2111.00254](#))
- [36] Rader J, Lyons T and Kidger P 2024 Optimistix: modular optimisation in JAX and Equinox (*Preprint* [2402.09983](#))
- [37] Kidger P 2021 *On Neural Differential Equations* Ph.D. thesis University of Oxford